

Non-Zeeman Circular Polarization of Molecular Spectral Lines in the ISM

Mohammed Afif Chamma

May 27, 2018

Submitted in partial fulfillment
of the requirements for the degree
of M.Sc. Astronomy

Supervised by Dr. Martin Houde
Department of Physics and Astronomy
University of Western Ontario
London, Ontario, Canada

Co-Authorship

The archival data that forms the basis of this work was reduced and provided by Dr. Ramprasad Rao, receiver support engineer at the Submillimeter Array (SMA) on Mauna Kea. The idea for and first version of the code that performs the correction necessary to eliminate false signals was provided by Dr. Josep Miquel Girart, who was visiting the SMA at the same time as I was. My supervisor, Dr. Martin Houde, provided extensive edits on several drafts of this paper and guidance on how to coax out the signals from the noise and display them in a clear way.

As for my role, I adapted Dr. Girart's code and used it to correct the archival data provided by Dr. Rao for four different astronomical objects. I created software built on top of the reduction package *Miriad* to efficiently collect data for and create the many figures and maps required to make the case that the signals we were presenting were true signals. Dr. Houde and I interpreted the data and detailed the arguments present in the paper to support the reliability of the signals. I was responsible for writing drafts of the paper and this report.

Contents

1	Introduction	4
1.1	Magnetic Fields through the Zeeman Effect	6
1.2	Magnetic Fields through Polarimetry	7
2	Research Methods	9
2.1	Radio Interferometry	10
2.2	Data Reduction with <i>Miriad</i>	14
2.3	Code Repositories	20
3	Non-Zeeman Circular Polarization of Molecular Spectral Lines in the ISM	21
4	Conclusion	32
5	Acknowledgments	32
6	References	33

1 Introduction

Stars form when clouds of gas and dust gravitationally collapse until they are hot enough to ignite fusion in their core. Assuming that gravity is the dominant force in the star formation process one can calculate several parameters of a molecular cloud such as the maximum mass stable against gravitational collapse (the Jeans mass), given by

$$M_J \simeq \left(\frac{5kT}{G\mu m_H} \right)^{3/2} \left(\frac{3}{4\pi\rho_0} \right)^{1/2}, \quad (1)$$

where T is the temperature of the cloud, ρ_0 is its initial density, and m_H is the mass of hydrogen. We can also find the free-fall timescale for such a collapse, given by (Carroll & Ostlie, 2006)

$$t_{ff} = \left(\frac{3\pi}{32G\rho_0} \right)^{1/2}. \quad (2)$$

However, the presence of turbulence and magnetic fields in a molecular cloud complicates star formation, either by slowing down the collapse or preventing it from happening at all. Developing methods for measuring and characterizing turbulence and magnetic fields in molecular clouds is therefore an important research focus in star formation. This report focuses on polarimetry, the dominant method for measuring the magnetic field.

The magnetic field in a molecular cloud can provide support against gravitational collapse and the strength of the field can determine the timescale at which collapse happens. The critical mass of a cloud with a magnetic field, while ignoring turbulence, is given by

$$M_\Phi = \frac{\Phi}{2\pi\sqrt{G}}, \quad (3)$$

where Φ is the magnetic flux in the cloud (Nakano & Nakamura, 1978; Crutcher, 2012). Clouds with masses below M_Φ are called subcritical and are supported against collapse by the magnetic field, while supercritical clouds with a mass higher than M_Φ

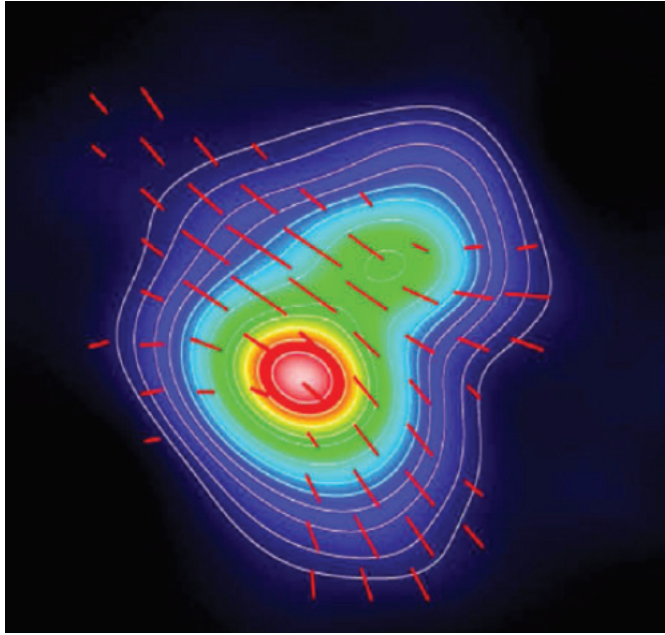


Figure 1: A map of NGC1333 IRAS4A made with the Submillimeter Array (SMA). Colours and contours show levels of continuum dust emission (red pixels show higher intensity). The red vectors show the direction of the magnetic field in the plane of the sky (Girart, Rao, & Marrone, 2006).

will collapse and form stars (Nakano & Nakamura, 1978; Crutcher, 2012). In clouds that are subcritical ions are locked to the magnetic field lines and only neutral gas and dust can collapse into the core of the cloud, eventually causing its mass to increase and become supercritical (Crutcher, 2012). In clouds with weak fields the mass is already supercritical and turbulence plays a larger role in driving collapse (Crutcher, 2012).

These theoretical models make several observable predictions. The simplest is that regions with strong fields will have smooth field lines throughout all stages of the cloud’s collapse (Crutcher, 2012). Also, collapsing clouds that are supported by strong magnetic fields will form oblate spheroids since the cloud has more support along the direction perpendicular to the field. In addition, a region with initially parallel field lines will begin to “pinch” as the cloud collapses, creating an hourglass morphology (Crutcher, 2012). An example of this hourglass can be seen in Figure 1.

Understanding the details of the star formation process is a driving force for developing the methodology of measuring magnetic fields around star-forming regions and the interstellar medium. In astronomy, new tools for observing the universe frequently reveal surprising results and open doors into future research fields, and this methodology is no exception.

1.1 Magnetic Fields through the Zeeman Effect

The Zeeman effect makes it possible under certain conditions to directly measure the magnetic field strength along the line of sight in a molecular cloud, and it also has a unique polarization signature (Crutcher, 2012). The presence of a magnetic field can cause the spectral line of a molecule to split into several components, where the size of the split is proportional to the strength of the magnetic field (Zeeman, 1897). For the Zeeman effect to be used to measure the interstellar magnetic field the presence of Zeeman-sensitive molecules is necessary. The size of the split $\Delta\nu_Z$ in the spectral line is given by

$$\Delta\nu_Z = Z|B|, \quad (4)$$

where B is the magnetic field strength, and Z is called the Zeeman factor and depends on the molecule and transition in question (Crutcher, 2012). The Zeeman effect has only been detected in the interstellar medium in the lines of HI, OH, and CN, since most other common species have very small Z factors (Crutcher, 2012).

When a spectral line splits it splits into three components that each have a different polarization signature. The central component is called the π -component, which is unshifted in frequency, and is linearly polarized parallel to the component of B along the plane of the sky (B_{POS}). The other two components are the σ -lines which, on either side of the central π -component, are oppositely circularly polarized along the line-of-sight (if the field has a component B_{LOS} in that direction) and

linearly polarized perpendicular to B_{POS} . In principle by measuring the size of the split and the full polarization state of the three components one can obtain full information about \vec{B} (Crutcher, 2012). However, except for OH masers in a few cases, the Zeeman split is usually smaller than the linewidth of the spectral line, which limits the amount of information that can be obtained to B_{LOS} (Crutcher, 2012). In addition, for molecules with small Z factors, no net circular polarization is expected from the Zeeman effect since the σ -components, which are equal in strength and opposite in polarization, overlap (Crutcher, 2012). For this reason the discovery of circular polarization in the molecule CO was surprising and required a different mechanism to explain it, in view of its extremely low sensitivity to the Zeeman effect (Houde et al., 2013; Houde, 2014).

1.2 Magnetic Fields through Polarimetry

Maps of the magnetic field like that shown in Figure 1 are made by measuring the polarization state of the light incident on a telescope. At millimetre and submillimetre wavelengths, inferring the magnetic field from the measured polarization state is usually done either through broadband measurements of continuum thermal dust emission or using rotational transitions of molecules, like CO. Measuring molecular transitions has the advantage of brighter intensities compared to measuring thermal dust emission. In addition, by selecting different molecules we can obtain information on gas dynamics and detail about the structure of the cloud. This section will give a brief overview of the two methods and will give context to certain challenges with polarimetry of molecular spectral lines that the work presented here highlights.

The mechanisms that give rise to polarized light from dust versus from molecules are, though different, both related to the presence of a magnetic field in the local environment. It is generally expected that dust grains align themselves with their long axis perpendicular to the magnetic field due to asymmetric radiative torques, causing

any thermal emission from long grains to be linearly polarized perpendicular to the field (Andersson et al., 2015). Molecules will also preferentially align to the magnetic field because of the magnetic moment associated with their rotational transitions. In addition, a molecule in a magnetic field in a medium subjected to some anisotropy (e.g., in the ambient radiation field or the optical depth) will exhibit a net linear polarization level due to the resulting imbalance in the populations of the levels leading to the π - and σ -lines (Goldreich & Kylafis, 1981; Crutcher, 2012). This is referred to as the Goldreich-Kylafis (GK) effect and results in molecules emitting a small percentage of radiation that is linearly polarized either perpendicular or parallel to the plane of the sky component of the magnetic field B_{POS} (Goldreich & Kylafis, 1981). The degeneracy in the direction of the magnetic field is usually resolved by measuring continuum emission along with molecular emission, or by measuring several molecular transitions (Crutcher, 2012).

If we imagine molecules in a cloud subject to the effects of both a local magnetic field and turbulent motion, then we would expect that the stronger the magnetic field is relative to the turbulence in that region the lower the dispersion in polarization angles (PAs), since turbulence has the effect of disturbing the orientation of the field. Therefore if we observe a large dispersion in PAs in a region then we might conclude that the field there is weaker than in a region where the PAs are more uniform, assuming the same level of turbulence. This idea is formally expressed by the Davis-Chandrasekhar-Fermi (DCF) method where the measured dispersion of PAs and particle velocities can be used to calculate the strength of the plane of the sky component of the magnetic field according to

$$B_{POS} = \sqrt{4\pi\rho} \frac{\delta V}{\delta\phi}, \quad (5)$$

where ρ is the gas mass density, δV is the velocity dispersion of the particles in

the cloud (and is a measure of the level of turbulence) and $\delta\phi$ is the dispersion in PAs (Davis, 1951; Chandrasekhar & Fermi, 1953; Crutcher, 2012). This method has proven useful in estimating the magnetic field in molecular clouds and in the galactic plane (Chandrasekhar & Fermi, 1953; Crutcher, 2012), and has seen several extensions and refinements in recent years (Houde, 2004; Hildebrand et al., 2009; Houde et al., 2009).

Since the PA is the critical piece of information that connects polarization measurements to the orientation of the magnetic field, any effects that change the PA will taint the measurement of the magnetic field. Two important examples of this that concern this report are the presence of polarized light due to the telescope's instrumentation (e.g.: Hamaker et al., 1996; Sault et al., 1996; Marrone et al., 2008) and anisotropic resonant scattering (ARS) from molecular transitions, which can convert linear polarization (LP) to circular polarization (CP) along the line of sight (Houde et al., 2013; Hezareh et al., 2013; Houde, 2014). Since it may be possible to retrieve the ‘lost’ LP by measuring CP (Hezareh et al., 2013), and the ARS effect may be a common occurrence in molecular clouds (this work), measuring CP simultaneously with LP when doing molecular spectral line polarimetry may be essential to obtaining accurate measurements of the magnetic field.

2 Research Methods

The data presented in the attached paper were collected from the archive of the Submillimeter Array (SMA), an array of eight 6m radio telescopes located at Mauna Kea, Hawaii. This section will describe the basic principles of radio interferometry, how polarimetric data is collected with the SMA, and an overview of the data reduction process using the *Miriad* data reduction package (Sault et al., 1995).

2.1 Radio Interferometry

Radio interferometry is a technique for obtaining high-resolution maps of objects in the sky that avoids building gigantic primary reflectors and relies on computationally intensive data analysis tasks.

Since the angular resolution of a telescope goes as $\theta \propto \lambda/D$, where λ is the wavelength and D is the diameter of the primary reflector, we try to build larger and larger mirrors and dishes to obtain higher resolution. However, reflectors that are large enough become very challenging to build when seeking resolutions of $< 1''$ at radio wavelengths. To illustrate how we can attain a higher resolution without building a massive reflector, consider a dish with a diameter 500 m across: this dish gives us high resolution but is beyond our ability to manufacture. Imagine now that we remove or obstruct large sections of this reflector. The images we would obtain from such a “patchy” reflector are now in fact the Fourier transform of the intensity map of the object being examined on the sky, much like how the support struts on, for example, Hubble, cause imaged stars to appear to have a superimposed cross pattern. With radio interferometry, we obtain the resolution of a large dish by sampling the light it would receive and inferring the true sky image by inverting the measured Fourier transform.

The resolution of the interferometer array is determined by the longest baseline separation B_{max} between any two elements of the array. This B_{max} is effectively the diameter of our “patchy” reflector. However, while the resolution defines the scale of the smallest object that is resolvable, an interferometer also has a limit on the largest resolvable scale, which is defined by the shortest baseline B_{min} of any two elements in the array. This implies that large-scale spatial emission will be filtered out by the interferometer.

The output of a radio interferometer is the visibility function $\mathcal{V}(u, v)$, which is found by correlating the voltage signals from all pairs of antennae. This correlation is

done on-the-fly by an onsite computer, the so-called correlator, and the raw voltage signals are often discarded after the correlation is computed due to the prohibitively large amount of data. The arguments u and v are called the spatial frequencies and measure the distance between the two antennae in wavelengths. Given antennae a and b the visibility is written as

$$\mathcal{V}(u, v) = \frac{\langle V_a(t) \star V_b(t) \rangle}{A_0 \Delta\nu}, \quad (6)$$

where $V_a(t)$ and $V_b(t)$ are the measured voltage signals from antennae a and b , A_0 is the collecting area of the dish, $\Delta\nu$ is the bandwidth of the receiver, and $\langle V_a(t) \star V_b(t) \rangle$ denotes the time-averaged cross-correlation of the voltage signals, which is defined by

$$\langle V_a(t) \star V_b(t) \rangle = \lim_{T \rightarrow \infty} \frac{1}{2T} \int_{-T}^T V_a(t) V_b^*(t - \tau) dt. \quad (7)$$

Here τ is a delay parameter that is chosen based on the type of observations being made (Thompson et al., 2001).

The expression shown in eq. (6) can be shown to be equivalent to the Fourier transform of the intensity map (the image) $I(l, m)$, where l and m are angular positions, through the van Cittert-Zernicke theorem. In its most general form the van Cittert-Zernicke theorem proves that incoherent radiation observed from a large distance appears to be coherent (see Chap. 14 of Thompson et al., 2001, for a derivation). Here we prove a consequence of it as it relates to interferometry to show that $\mathcal{V}(u, v) = \mathcal{F}\{I(l, m)\}$, where $\mathcal{F}\{\}$ denotes the Fourier transform.

Consider two antennae a and b at positions (x_a, y_a) and (x_b, y_b) , pointed at the same object. The electric field at antennae a and b from sky position (l, m) at time t is given by

$$E_a(l, m, t) = A(l, m, t) e^{i\phi(l, m, t) + i\frac{2\pi}{\lambda}(x_a l + y_a m)} \quad (8)$$

$$E_b(l, m, t) = A(l, m, t) e^{i\phi(l, m, t) + i\frac{2\pi}{\lambda}(x_b l + y_b m)}, \quad (9)$$

where λ is the wavelength of observation, $A(l, m, t)$ is the amplitude of the field and $\phi(l, m, t)$ is the phase of the wave, which van Cittert-Zernicke tells us is the same in both $E_a(l, m, t)$ and $E_b(l, m, t)$ since the waves appear as coherent. The total voltage response of the antenna's receiver is the superposition of all electromagnetic waves from each position of the object, which can be written as:

$$V_a(t) = \int_{l,m} E_a(l, m, t) dl dm = \int_{l,m} \int_{\nu} E_a(l, m, \nu) e^{2\pi i \nu t} d\nu dl dm \quad (10)$$

$$V_b(t) = \int_{l,m} E_b(l, m, t) dl dm = \int_{l,m} \int_{\nu} E_b(l, m, \nu) e^{2\pi i \nu t} d\nu dl dm, \quad (11)$$

where we chose to express $E(l, m, t)$ in terms of its Fourier transform. We will also write $E(l, m, \nu) = A(l, m, \nu) e^{i\phi(l, m, \nu)} e^{i\frac{2\pi}{\lambda}(xl + ym)}$. The complex product is now

$$\begin{aligned} V_a(t)V_b^*(s) &= \int_{l,m} \int_{\nu} E_a(l, m, \nu) e^{2\pi i \nu t} d\nu dl dm \times \int_{l',m'} \int_{\nu'} E_b^*(l', m', \nu') e^{-2\pi i \nu' s} d\nu' dl' dm' \\ &= \int_{l,m} \int_{l',m'} \int_{\nu} \int_{\nu'} A(l, m, \nu) A^*(l', m', \nu') e^{i\phi(l, m, t) + i\frac{2\pi}{\lambda}(x_a l + y_a m)} \\ &\quad e^{-i\phi(l', m', \nu') - i\frac{2\pi}{\lambda}(x_b l' + y_b m')} e^{2\pi i \nu t} e^{-2\pi i \nu' s} d\nu d\nu' dl' dm' dl dm \\ &= \int_{l,m} \int_{l',m'} \int_{\nu} \int_{\nu'} A(l, m, \nu) A^*(l', m', \nu') e^{i\phi(l, m, \nu) - i\phi(l', m', \nu')} \\ &\quad e^{i\frac{2\pi}{\lambda}(x_a l - x_b l' + y_a m - y_b m')} e^{2\pi i(\nu t - \nu' s)} d\nu d\nu' dl' dm' dl dm \\ &= \int_{l,m} \int_{\nu} |A(l, m, \nu)|^2 e^{2\pi i \nu(t-s)} e^{i\frac{2\pi}{\lambda}(\Delta xl + \Delta ym)} d\nu dl dm, \end{aligned} \quad (12)$$

where the last line follows since

$$\int_{l,m} \int_{l',m'} \int_{\nu} \int_{\nu'} e^{i\phi(l, m, \nu)} e^{-i\phi(l', m', \nu')} d\nu d\nu' dl dm dl' dm' = \delta(\nu - \nu', l - l', m - m'), \quad (13)$$

and the other terms are constant relative to the $e^{i\phi}$ terms. This is because even though both antennae measure the same phase $\phi(l, m, \nu)$, it varies extremely quickly

across different spatial positions l and m , and frequency ν . The positional arguments of the antennae are related to the spatial frequencies u and v by

$$u = \frac{\Delta x}{\lambda} = (x_a - x_b)/\lambda \quad (14)$$

$$v = \frac{\Delta y}{\lambda} = (y_a - y_b)/\lambda. \quad (15)$$

If we now set $s = t - \tau$, where τ is the time lag set by the correlator then we have

$$V_a(t)V_b^*(t - \tau) = \int_{l,m} \int_{\nu} |A(l, m, \nu)|^2 e^{2\pi i \nu \tau} e^{2\pi i (ul + vm)} d\nu dl dm, \quad (16)$$

After time-averaging according to eq. (7) we finally obtain

$$\begin{aligned} \langle V_a(t)V_b^*(t - \tau) \rangle &= \lim_{T \rightarrow \infty} \frac{1}{2T} \int_{-T}^T \int_{l,m} \int_{\nu} |A(l, m, \nu)|^2 e^{2\pi i \nu \tau} e^{2\pi i (ul + vm)} d\nu dl dm dt \\ &= \int_{l,m} \int_{\nu} I(l, m, \nu) e^{2\pi i \nu \tau} e^{2\pi i (ul + vm)} d\nu dl dm \\ &= \mathcal{F}\{I(l, m, \nu)\}, \end{aligned} \quad (17)$$

where $I(l, m) = |A(l, m)|^2$ (chap. 3 of Thompson et al., 2001; Vanderlinde, 2017).

Thus at a given frequency of observation ν we can say that $\langle V_a(t)V_b^*(t - \tau) \rangle_{\nu} = \mathcal{F}\{I(l, m, \nu)\}$.

Equation (17) shows the Fourier transform connection between the cross-correlation and the intensity map $I(l, m)$. The intensity map is therefore obtained by performing an inverse 2D Fourier transform on the visibilities, which is of course limited by how well the visibilities have been measured. A single pair of antennae samples a single (u, v) point in visibility space, meaning that the more baselines there are in the array the better the uv -coverage and the more accurate the final map is. The uv -coverage is also greatly improved by the rotation of the Earth since different orientations relative to the object change the (u, v) coordinates (Thompson

et al., 2001). Images formed from poorly sampled visibilities will result in a large number of periodic ‘blobs’ or ‘stripes’ on the image that are not real and are purely a side-effect of the periodic functions used to perform the Fourier transform.

To obtain maps at different frequencies the signal must be binned into different spectral channels before being correlated. To obtain maps of specific polarizations in addition to different frequencies, either receivers sensitive to different polarizations must be used (like at ALMA) or the observing time is split so that the receivers are exposed to light of different polarization states. The SMA uses the latter strategy and uses a quarter-wave plate (QWP) in the beam of each antenna to sample the two polarization states: left-CP (LCP) and right-CP (RCP). Each antenna can only sample one polarization state at a time, and the QWP is rotated 90° to sample the other state. To obtain full polarimetric information for the visibilities from a single baseline, the two antennae must correlate their responses to all combinations of polarization states (Hamaker et al., 1996; Sault et al., 1996; Thompson et al., 2001; Marrone et al., 2008). That is, if an antenna can sample polarization states ‘ L ’ and ‘ R ’ (which corresponds to 90° rotations of the QWP), then, for a pair of antennae, four correlations must be found: LL , LR , RL , and RR . On the SMA this is done by rotating the QWPs on both antennae in a cycle that repeats every 4-6 minutes (Marrone et al., 2008). Figure 2 shows the SMA’s QWP assembly.

2.2 Data Reduction with *Miriad*

The data reduction package *Miriad* (Sault et al., 1995) implements and performs most of the required computational tasks for calibrating the data and performing an inverse Fourier transform to obtain maps. When observations are taken the intensity of the visibilities is usually calibrated against measurements of quasars that are taken during the same night, since certain quasars can be assumed to be steady, bright, unchanging sources. This involves calculating gain coefficients to correctly scale the

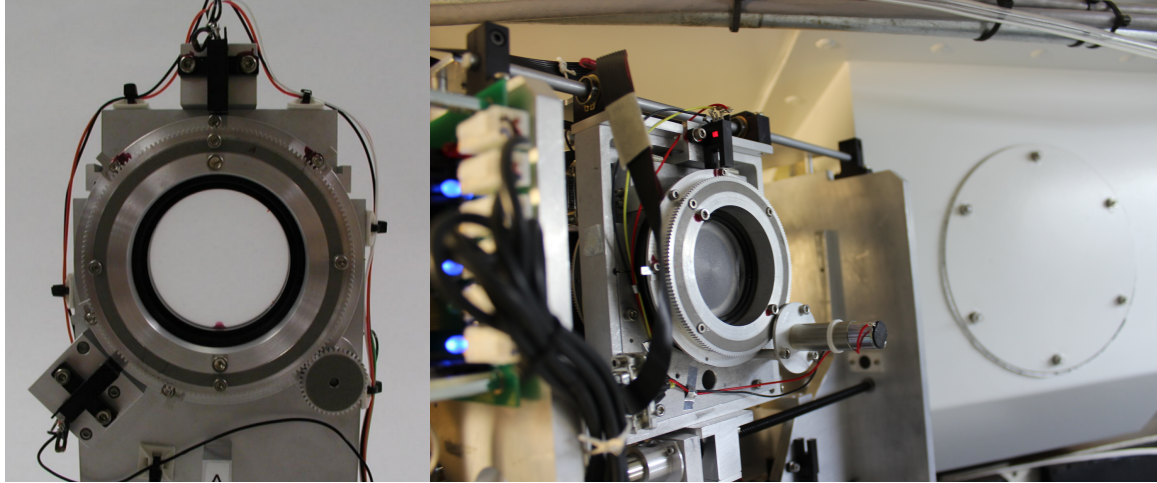


Figure 2: (*left*) The SMA’s quarter-wave plate (QWP) mounted on a rotation stage. Optical brakes (top and bottom left) determine the position of the QWP. Adjustable flags (small screws on perimeter of the rotation stage) at $\pm 45^\circ$ from the top optical brake set the positions of the waveplate (from Fig. 1 of Marrone et al., 2008). (*right*) The QWP mounted inside the cabin of an SMA antenna in the path of the beam (personal photo).

visibilities to their true intensities. The data presented in this paper were already calibrated by Dr. Rao and Dr. Girart, and so the calibration process will not be explained in detail here. In *Miriad*, programs that perform useful operations on the data are broken up into commands called ‘tasks’ which can be scripted using bash scripts or Python. This section will summarize the most important tasks for creating images from the visibilities.

The `invert` task performs a standard two-dimensional fast Fourier transform (FFT) on a grid whose size can be specified by the user (Sault et al., 2008). It also generates a beam map that gives the response of the interferometer to a point source based on the location of the antennae in the array and the frequency being observed. The beam map is necessary because `invert` alone tends to produce maps of objects that are filled with sidelobes: bumps, peaks, and stripes that arise in the map when the *uv*-coverage of the array is irregular, called the “dirty” map (Högbom, 1974; Thompson et al., 2001; Sault et al., 2008). In interferometry the *uv*-coverage is often irregular due to the fact that the placement of dishes is limited to the geography

of the region (as on Mauna Kea for the SMA) and specific dishes often need to be excluded from the data due to malfunction (Högbom, 1974). The beam map, because it is made with observations of a point source, can tell us what the pattern of sidelobes is and makes it possible to deconvolve the sidelobe pattern from the dirty map, leaving behind the approximately real structure. This process is called Högbom iteration (Högbom, 1974) or ‘CLEAN’ and is implemented by the `clean` task in *Miriad* (Sault et al., 2008).

The `clean`-ing of the dirty map is performed by subtracting the entire dirty beam from the position where the dirty map is maximum. The amplitude of the dirty beam is usually normalized to be a fraction of the maximum of the dirty map, called the loop gain (Högbom, 1974). This subtraction is repeated on what remains of the map until nothing is left. A model is then built by placing point sources at all the positions where a peak was removed at the corresponding amplitude that it was removed at. By then analytically calculating a “clean” beam, which is the response to a point source given the diameter of a single dish, the model can be convolved with the clean beam using the `restor` task to obtain a clean map (Högbom, 1974; Thompson et al., 2001; Sault et al., 2008). Figure 3 demonstrates the `clean`-ing process on the IRC+10216 data presented in the attached paper. Note that the CLEAN algorithm works on extended sources like nebulae or molecular clouds by modelling them as a collection of point sources (Högbom, 1974).

Another task critical to the results presented in the paper is `selfcal` (self-calibration), which makes additional corrections to the gain calibration of the data (Sault et al., 2008). As explained in the paper, this is necessary to correct the very small offset between beams of different polarizations that leads to false Stokes V signals. The `selfcal` task takes the clean model found from `invert`-ing and `clean`-ing the initial visibilities and uses it to find new gain coefficients that better fit the model. The gain coefficients can be further improved by repeating the self-calibration

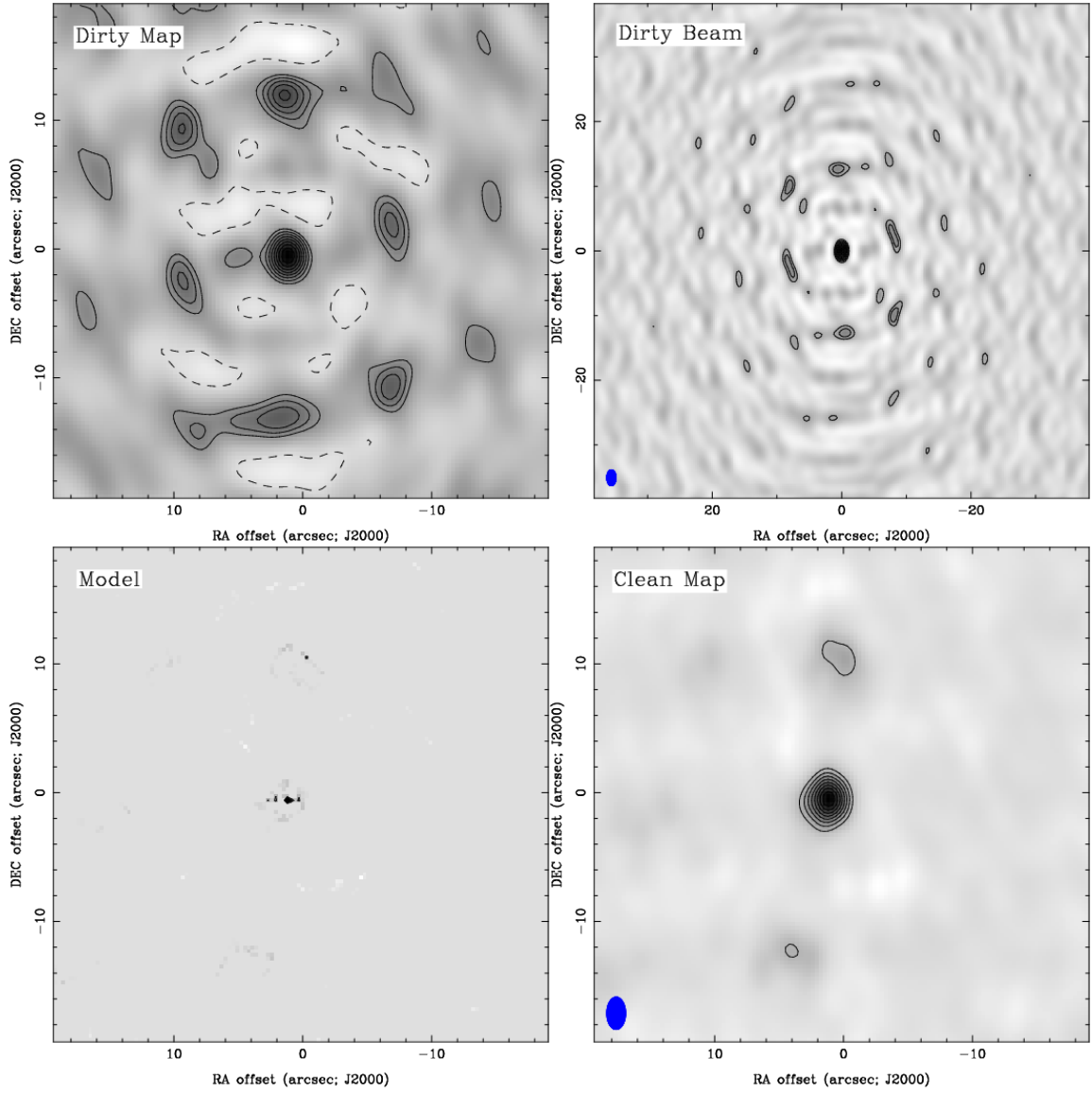


Figure 3: The dirty map (**top left**), dirty beam (**top right**), model obtained from the clean task (**bottom left**), and deconvolved CLEAN map of IRC+10216 (**bottom right**). Contour levels are at -20%, 20%, 30%, 40%, etc. of the maximum. Negative contours are dashed. Pixels show the same data, and darker pixels represent higher intensity. Notice the six peaks around the larger central peak in the dirty map that are also present in the dirty beam but are largely absent in the clean map.

process on a new model generated from the last gain coefficients to be found (Sault et al., 2008). The gain coefficients (which are complex-valued) are searched for and found iteratively by minimizing the following error heuristic

$$\epsilon^2 = \sum |\mathcal{V}_{ab} - g_a g_b^* \hat{\mathcal{V}}_{ab}|^2, \quad (18)$$

where \mathcal{V}_{ab} are the measured visibilities found by correlating signals from antenna a and b , $\hat{\mathcal{V}}_{ab}$ are the model visibilities for the same baseline, and g_x are the complex gain coefficients (Schwab, 1980; Sault et al., 2008). By finding the gain coefficients that minimize eq. (18), `selfcal` adjusts the measured visibilities until they match the model, and, when models are regenerated after each iteration of `selfcal`, the gain coefficients eventually converge and further iterations do not improve the image (Schwab, 1980; Sault et al., 2008). The self-calibration process can also be applied on visibilities with different polarizations, which is what allows us to correct the offset in each polarized beam.

While *Miriad*'s tasks make it easy to create scripts to automate data reduction and correct the data, the tasks themselves take parameters that must be manually found based on the data set being used, and are usually different for different objects. Using *Miriad* to search the data for Stokes V signals was initially a monumental challenge since our archive search started with over 25 different sets of data of different celestial objects taken with different spectral configurations. For example, an early step in the `invert-ing` process is to average the spectral channels that make up a spectral line (e.g. CO ($J = 3 \rightarrow 2$) at 345.8GHz) so that the inversion process completes successfully. This is done by specifying the number of channels to end with after averaging, the velocity (in km/s) of the channel to start averaging at, and the number of channels to merge together. This involved manually opening the spectra of interest, counting the correct number of channels to cover the entire line, and then

switching the x-axis of the displayed spectra to find the corresponding velocity of the starting channel. These values are then passed to the `invert` task like so:

```
1 invert line=vel,18,-43,2,2 vis=[...]
```

where the format is `line=vel,{# of channels},{starting channel},{step},{# to merge}`. The `invert` task has a bug where if the step size does not agree with a hidden rule I was unable to ascertain, it would fail, requiring you to increase the step size and manually recount the number of channels to input as the first number. Since each dataset required a correction script to be written for it, and we wanted to search as much data as possible, inefficiencies like the example above quickly made progress difficult and cumbersome.

To improve the workflow and automate little menial details like counting it was necessary to automate parameter generation for *Miriad*'s tasks. In a language like bash, which *Miriad* supported scripting for natively, such automation would bring its own cumbersome details, and it became clear a language like Python would be better suited for the task. No Python wrapper existed for *Miriad* so I created one and used it to generate any tedious parameters needed for any of the *Miriad* tasks, including detecting when `invert` fails due to the mysterious step bug and automatically changing the step size until the task completes. Other notable features include dumping spectral information to the terminal and parsing it in Python for information needed to generate other parameters, counting channels automatically, displaying a window with a spectrum that outputs channel information on mouse click, and, in general, allowing one to take advantage of the language features of Python such as loop structures, function definitions, and string substitution. For example, the Python method used to automate the line selection parameter for `invert` is the following:

```
1 def averageVelocityLine(vis, factor):
2     velrange = getVelocityRange(vis)
3     nvels = round(abs(velrange[0] - velrange[1])/factor)
4     startvel = round(velrange[1])
5     return 'vel,{0},{1},{2},{2}'.format(nvels, startvel, factor)
```

which, under the hood, gets the velocity range of the line by using the output of the `uvlist` task in *Miriad* and parsing it for the velocity range before using it to compute the necessary number of channels and building the necessary string in the format that *Miriad* expects.

The Python *Miriad* wrapper works by generating the necessary bash command to run and then passing the command to the terminal. Depending on the task, the output can be displayed in the terminal as usual or can be intercepted by Python and used for other tasks.

Having a Python interface to *Miriad* also made it possible to connect the data to the plotting utilities available in Python, such as `matplotlib` (Hunter, 2007), and also allowed easier access to *Miriad*'s own plotting utilities like `cgdisp` which is used to display contour plots of maps.

Creating an automation suite for *Miriad* in Python and connecting it directly to several different custom plotting methods made it possible to correct more data, find potential Stokes V signals across different spectral lines more efficiently, and create the many figures and maps required to convince ourselves of whether the signals were real or not.

2.3 Code Repositories

All of the code that performs the data reduction, squint correction, and plotting is available online.

The data analysis and correction scripts can be found at github.com/mef51/SMAData. This repository contains all the archival polarimetric data from the SMA (analysis scripts only). The folders relevant to this paper are `IRC+10216/`, `080106_Ram_Spectra/` (for Orion KL), `141028_ngc7538/` (for NGC7538), and `101014_NGC1333_Ram/` (for NGC1333).

Within that repository is the `squintscripts/` folder which contains all the scripts

for generating the figures included in the paper, as well as some extra figures. The `paperplots.py` file contains some utilities for styling the figures. The `GetCOMaps.py` file generates all the maps used in the paper. `CompareImageSpectra.py` generates the before-and-after correction comparison of the spectra (Figure 4 of the attached paper).

The Python wrapper for *Miriad* described in the previous section is provided in a separate repository due to its potential use for others and can be found at github.com/mef51/smautils. It contains the wrapper as well as a library (`squint.py`) for performing the squint correction detailed in the paper. It is published on the Python Package Index (PyPi) and can be installed by anyone by running the command ‘`pip install smautils`’ on the terminal.

3 Non-Zeeman Circular Polarization of Molecular Spectral Lines in the ISM

The following paper has been submitted for publication to *Monthly Notices of the Royal Astronomical Society* (MNRAS).

NON-ZEEMAN CIRCULAR POLARIZATION OF MOLECULAR SPECTRAL LINES IN THE ISM

MOHAMMED AFIF CHAMMA¹, MARTIN HOUDE¹, JOSEP MIQUEL GIRART² AND RAMPRASAD RAO³

¹Department of Physics and Astronomy, The University of Western Ontario, London, ON, N6A 3K7, Canada

²Institut de Ciències de l'Espai (IEEC-CSIC), Can Magrans, S/N, E-08193 Cerdanyola del Vallès, Catalonia, Spain
and

³Submillimeter Array, Academia Sinica Institute of Astronomy and Astrophysics, 645 N. Aohoku Place, Hilo, HI 96720, USA

Abstract

We searched archival data of the Submillimeter Array (SMA) for evidence of circular polarization in common molecular tracers, most notably CO. This circular polarization possibly arises from anisotropic resonant scattering, which would imply that some background linearly polarized flux is being converted to circular polarization. We find circular polarization in NGC7538 (in CO), IRC+10216 (in CS, SiS, H¹³CN and CO) and Orion KL (in CO and SiO) at high enough levels to suggest that the presence of circular polarization in these spectral lines is common for such objects. This would imply that an important piece of information has been neglected when studying magnetic fields through linear polarization from molecular spectral lines in the interstellar medium.

Keywords: circumstellar matter - ISM: clouds - polarization - magnetic fields

1. INTRODUCTION

Understanding the role of magnetic fields in star-forming regions allows us to test ideas about free-fall collapse and support mechanisms in molecular clouds, filling in details about the star formation process. By measuring the radiation from star-forming regions astronomers use polarimetry to infer the magnitude and orientation of the magnetic field. The Davis-Chandrasekhar-Fermi (DCF) method (Davis 1951; Chandrasekhar & Fermi 1953) uses the dispersion of polarization angles (PA) of linear polarization (LP) for measuring the plane-of-the-sky component of the magnetic field. The presence of a magnetic field leads to LP radiation because dust and molecules will align themselves relative to the field. Aligned particles can emit radiation with a net level of LP greater than zero. Aligned dust can also absorb radiation whose polarization is aligned with its long axis, acting as a sort of polarizing grid. Thus measuring the amount of dust LP in the infrared continuum tells us about the degree to which the dust is aligned with the magnetic field, which in turn can tell us about the strength of the magnetic field (Davis 1951; Chandrasekhar & Fermi 1953; Crutcher 2012).

The alignment of molecules and their interaction with the ambient magnetic field can cause their transitions to be linearly polarized by a few percent through the so-called Goldreich-Kylafis (GK) effect (Goldreich & Kylafis 1981). LP due to the GK effect was first detected in CS ($J = 2 \rightarrow 1$) and HCN ($J = 1 \rightarrow 0$) in IRC+10216 and CRL 2688 by Glenn et al. (1997) and later in CO ($J = 3 \rightarrow 2$) and ($J = 2 \rightarrow 1$) by Greaves et al. (1999). Shortly after, LP from the GK effect was detected interferometrically for the first time and used to map the direction of the magnetic field in NGC1333 IRAS4A (Girart et al. 1999). As with dust, the PA associated with the LP in the spectral line can be measured and used to infer properties of the magnetic field through a dispersion analysis (Davis 1951; Chandrasekhar & Fermi 1953; Crutcher 2012). Observations in DR 21(OH) of LP in CO ($J = 2 \rightarrow 1$) were compared with simultaneous dust continuum polarization measurements to assess the accuracy in using the GK effect to probe the magnetic field (Lai et al. 2003; Cortes et al. 2005).

For molecular lines circular polarization (CP) is usually ignored, largely because of difficulty in its measurement and its assumed irrelevance. However, a significant amount of unexpected circular polarization was reported by Houde et al. (2013) in CO ($J = 2 \rightarrow 1$), a common tracer through LP of magnetic fields (Crutcher 2012), using FSPPol (Hezareh et al. 2010) at the Caltech Submillimeter Observatory (CSO). The presence of CP in a molecular transition can be explained with Zeeman splitting for some molecules/transitions possessing a significant magnetic moment (e.g., CN), but CO is highly insensitive to the Zeeman effect. In addition, the

observed Stokes V profile in Orion KL was positive and symmetric, which is also unexpected since Zeeman splitting often gives rise to an approximately antisymmetric Stokes V profile. To explain this detection a model was proposed whereby background LP radiation is converted to CP radiation through anisotropic resonant scattering (ARS) (Houde et al. 2013; Houde 2014). This was further tested in the supernova remnant IC443 by Hezareh et al. (2013), where the measured CP flux of CO lines ($J = 2 \rightarrow 1$) and ($J = 1 \rightarrow 0$) were ‘re-inserted’ into the measured LP flux to account for the LP-to-CP conversion and its effect on the PA. They found that the PAs obtained from the different CO transitions only agreed with each other and with those obtained from dust polarimetry after the CP flux was accounted for. If ARS is common to other objects then using LP in CO as a tracer of the magnetic field will introduce a systematic error unless the CP of CO lines is also measured.

The main goal of this paper is to find further evidence of CP in more objects and molecular lines through a search of archival data of the Submillimeter Array (SMA¹). In Section 2 we discuss the issues that arise when doing polarimetry with radio interferometry, focusing specifically on circular polarization (CP). Section 3 will give in detail our scheme for correcting a spurious source of CP that arises with the SMA. Section 4 presents archival observations of four objects made with the SMA on Mauna Kea and investigates the reliability of our CP detections. Finally, in Section 5 we will highlight the significance of these CP detections and summarize their implications.

2. MEASUREMENT OF CP WITH RADIO INTERFEROMETRY

The measurement of CP is challenging to calibrate, especially when using radio interferometers like the SMA or ALMA. The SMA, which has linear feeds, uses a quarter-waveplate (QWP) in the path of the antenna beam to convert incident LP light to CP light to measure LP signals before sending them to the correlator. While not its most common use at the SMA the QWP can work the other way to measure CP: incident CP is converted to LP and then measured by the receivers. On the other hand, ALMA which also has linear feeds does not use a QWP and measures LP signals directly. While both types of feeds can be used to measure CP, the calibration process is different (Sault et al. 1996). Despite the calibration challenges the SMA has been used to take precise measurements of CP from dust continuum in Sgr

A* (Muñoz et al. 2012). For a discussion on measuring CP with radio interferometry and on design choices at the SMA (such as the choice of converting from LP-to-CP and vice-versa) see Hamaker et al. (1996) and Marrone et al. (2008).

2.1. Linear vs. Circular Feeds

To illustrate briefly the differences between the two feed types consider the following: with an orthogonal CP basis, the Stokes V parameter for a beam of radiation is defined by $V \propto \langle E_L^2 \rangle - \langle E_R^2 \rangle$, where E_L and E_R are the left-CP and right-CP electric fields, respectively. With an orthogonal LP basis Stokes V is defined by $V \propto -2\text{Im}(E_x E_y^*)$, where E_x and E_y are the LP fields, and $\text{Im}()$ denotes the imaginary part. In the CP basis case we take the difference of two measured intensities, while the linear feed case requires us to measure the phase of the electromagnetic wave.

Now, when the measurement is made with interferometry it is the visibilities – the correlated waveforms between a pair of antennae – that are measured. In the CP basis case the Stokes V visibility scales as $\mathcal{V}_V \propto \mathcal{V}_{RR} - \mathcal{V}_{LL}$, where \mathcal{V}_{RR} and \mathcal{V}_{LL} are the visibilities obtained from correlating two antennae measuring right-CP and left-CP, respectively (see eq. (3) below). In the linear feed case the Stokes V visibility is coupled with the Stokes Q and U visibilities (see Section 4.1 of Thompson et al. 2001). This means the Stokes Q and U of any calibration object must be measured as well. This is not possible with the SMA setup used for the observations discussed here.

3. SQUINT CORRECTION

We now describe spurious Stokes V signals that can arise during observations such as those presented here and our scheme for correcting them. This instrumental Stokes V comes from a slight pointing offset between the left- and right-handed CP beams.

The archival data used were in all cases observed with the goal of measuring LP (i.e., the Stokes Q and Stokes U parameters). As mentioned earlier on the SMA this is done with a QWP placed in front of the LP receivers to convert incident CP (LP) to LP (CP). While this method suffers from the errors that arise when subtracting two large measurements from each other, when performing CP measurements, it avoids having to solve for the LP terms of calibration objects (Marrone et al. 2008; Thompson et al. 2001).

The output of the interferometer is the visibility, which consists of the cross-correlation between the voltage signals from a pair of antennae and can be written as

$$\mathcal{V}(u, v) = \frac{\langle V_a(t) \star V_b(t) \rangle}{A_0 \Delta \nu}, \quad (1)$$

¹ The Submillimeter Array is a joint project between the Smithsonian Astrophysical Observatory and the Academia Sinica Institute of Astronomy and Astrophysics and is funded by the Smithsonian Institution and the Academia Sinica.

where A_0 is the collecting area of the antennae, $\Delta\nu$ is the bandwidth, and $\langle V_a(t) \star V_b(t) \rangle$ is the time-averaged cross-correlation of voltage signals $V_a(t)$ and $V_b(t)$ from antennae a and b , respectively. The arguments u and v are determined by the baseline separation and orientation of the two antennae. Thus a pair of antennae samples a single point of the visibility function $\mathcal{V}(u, v)$ (Thompson et al. 2001).

Through the van Cittert-Zernike theorem it can be shown that the visibility function $\mathcal{V}(u, v)$ gives the Fourier transform of the source intensity $I(l, m)$ for angular position l and m (chap. 3 of Thompson et al. 2001). Thus we have

$$\mathcal{V}(u, v) = \int \int e^{-iul} e^{-ivm} I(l, m) dl dm. \quad (2)$$

Given antennae a and b , the Stokes V visibility in the circular feed case is given by (Thompson et al. 2001; Muñoz et al. 2012)

$$\mathcal{V}_V \simeq \frac{1}{2} \left\{ \mathcal{V}_{RR}/(g_{Ra}g_{Rb}^*) - \mathcal{V}_{LL}/(g_{La}g_{Lb}^*) \right\}, \quad (3)$$

where \mathcal{V}_{RR} and \mathcal{V}_{LL} are the right-handed CP and left-handed CP visibilities, respectively, measured by appropriately orienting the QWP that is placed in the beam of the antennae and correlating their responses (Marrone et al. 2008). The complex gain factors for each polarization for each antenna are g_{Ra} , g_{Rb} , g_{La} and g_{Lb} where R and L are for right- and left-CP, respectively. Because the Stokes V visibility is found by taking the difference of two beams a slight offset gives rise to pairs of positive and negative peaks of Stokes V , as can be seen in Figure 1, for example. The cause of this offset is uncertain, but possibly arises due to slight differences in the index of refraction of the QWP when it is rotated.

To correct this offset we first note that since the visibilities are the Fourier transform of the intensity map (eq. 2), an offset in image space results in a complex factor in visibility space that can be absorbed into the gain coefficients. To see this, consider a map $I(l, m)$ that represents the true intensity I at angular position l and m . If the instrument introduces an arbitrary offset to position (l_0, m_0) , then the final image we calculate is shifted such that $I'(l, m) = I(l - l_0, m - m_0)$ and the measured visibility of the shifted map becomes

$$\begin{aligned} \mathcal{V}'(u, v) &= \int \int e^{-iul} e^{-ivm} I(l - l_0, m - m_0) dl dm \\ &= \int \int e^{-iu(\alpha+l_0)} e^{-iv(\delta+m_0)} I(\alpha, \delta) d\alpha d\delta \\ &= e^{-iul_0} e^{-ivm_0} \int \int e^{-iu\alpha} e^{-iv\delta} I(\alpha, \delta) d\alpha d\delta \\ &= e^{-iul_0} e^{-ivm_0} \mathcal{V}(u, v) \\ &\equiv g_{\text{offset}} \mathcal{V}(u, v), \end{aligned} \quad (4)$$

where we used the change of variables $\alpha = l - l_0$ and $\delta = m - m_0$. We thus find the aforementioned complex factor that multiplies the true visibility $\mathcal{V}(u, v)$. It is therefore easiest to correct for the offset in visibility-space by using *Miriad* (Sault et al. 1995) to solve for the gain coefficients on each of the two polarized beams, independently of each other. Specifically the process is:

1. The observations are calibrated for gain and phase in the usual way using observations of known sources (usually quasars like 3C84, 3C454, etc.; see *Miriad User Guide* (Sault et al. 2008)).
2. The visibilities are split into line-free continuum and line data. These are then mapped and used to obtain CLEAN models.
3. The separate continuum and line data are further split into *LL* and *RR* visibilities. *Miriad's self-cal* is used on the continuum data to solve for the gain coefficients of each antenna and each polarization (*L* or *R*). This is done by minimizing the difference between measured visibilities \mathcal{V}_{ij} of antennae i and j and model visibilities $\hat{\mathcal{V}}_{ij}$ according to $\epsilon^2 = \sum |\mathcal{V}_{ij} - g_i g_j^* \hat{\mathcal{V}}_{ij}|^2$ for each of the correlations *LL* and *RR* (Schwab 1980; Sault et al. 2008). The model visibilities used are those found earlier. Note the subscripts here denote a specific antenna and not the polarization state as before.
4. The gain found from the continuum *LL* data is then applied to the line *LL* data, and similarly for the *RR* continuum and line data.
5. The different visibilities (*LL*, *RR*, *RL*, *LR*) are recombined and inverted to produce corrected maps. Spectra can be obtained either from the corrected visibilities or the maps.

Figure 1 shows maps before- and after- correction maps for the continuum in Orion KL around 345GHz. We see that before correction there are large peaks of Stokes V , and that the three (identified) positive peaks have a negative peak close by. After the correction, though there are still noisy Stokes V signals throughout the image, the pairs of peaks have disappeared.

4. OBSERVATIONS

We collected radio interferometric polarimetry observations from the Submillimeter Array (SMA) archive that had been measured using the circular feeds, a similar setup to that used by Muñoz et al. (2012) to measure circular polarization from dust continuum in Sgr A*. Because the archival observations were not taken with measurements of CP in mind the SNR is often low, and we had to average velocity channels to increase it at

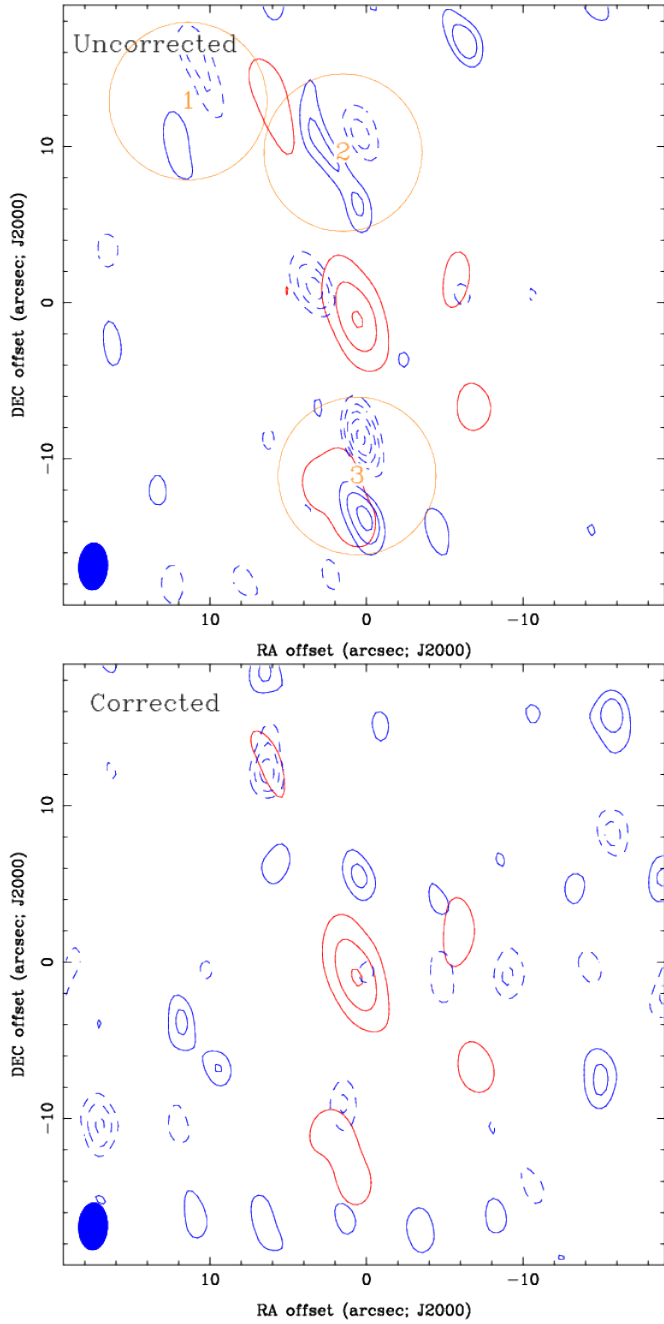


Figure 1. Map of the continuum around 345GHz in Orion KL before (top) and after (bottom) squint correction. Red contours are Stokes I , blue contours are Stokes V . Dashed lines denote negative values, solid lines denote positive values. Note the three pairs of positive and negative Stokes V peaks in the uncorrected map (identified and circled in orange). These largely disappear after correction. Red Stokes I contours are at 15%, 50%, and 95% of the peak intensity. Blue Stokes V contours are at $-8, -7, -6, -5, -4, -3, -2, 2, 3, 4, 5, 6, 7$ and 8σ levels.

the cost of spectral resolution. This generally increases the SNR from 3-4 to 6-10.

The four objects we present here are Orion KL, NGC7538, NGC1333 IRAS2A and IRC+10216. The first three are well-known star-forming regions, while

Object	Coordinates (J2000)	Array	Obs. Date
Orion KL	RA 05 ^h 35 ^m 14.501 ^s Dec -05°22'30.40"	Compact	2008-01-06
NGC7538	RA 23 ^h 13 ^m 44.771 ^s Dec +61°26'48.85"	Compact	2014-10-28
IRC+10216	RA: 09 ^h 47 ^m 57.381 ^s Dec +13°16'43.70"	Compact	2009-11-24
NGC1333	RA 03 ^h 28 ^m 55.580 ^s Dec +31°14'37.10"	Compact	2010-10-14

Table 1. Summary of Archival Observations Used

IRC+10216 is an evolved carbon star. The data for Orion KL were previously used for a dust polarization study in Tang et al. (2010), and the data for IRC+10216 were previously used for spectral line polarimetry in Girart et al. (2012). The archival data for NGC1333 IRAS2A and NGC7538 used here have not been published before as far as we are aware. We find significant Stokes V signals in all objects except for NGC1333 IRAS2A. Table 1 shows a summary of the objects presented and related information.

The visibility data were corrected for beam squint, as explained in Section 3 in order to reduce spurious Stokes V signals. As previously mentioned squint typically causes distinct pairs of positive and negative peaks of Stokes V throughout the inverted image. The squint correction is confirmed visually by inspecting the Stokes V maps, where we see the pairs of peaks largely disappear.

Figures 2 and 3 show corrected Stokes I and Stokes V spectra (left) obtained at the peak of the CO ($J = 3 \rightarrow 2$) Stokes V signal on the corresponding maps (right). A comparison of Stokes V spectra before and after correction are shown in Figure 4. Notice in all cases the Stokes V signal decreases after squint correction. Stokes V can also be found in the average spectrum obtained from all the visibility data, though SNR is of $3-5\sigma$ significant in that case compared to approximately $6-10\sigma$ when the spectrum is taken at the peak of the inverted maps. The presence of a Stokes V signal in the visibilities indicates the detections are not simply the result of the inversion process that creates the maps. That is, the Stokes V signals are not due to sidelobes that appear when calculating the inverse Fourier transform of the visibilities. As can be seen in the maps, in general the peaks of Stokes I and Stokes V do not coincide.

In Orion KL (Fig. 2) the lines of CO ($J = 3 \rightarrow 2$ at 345.8 GHz) and SiO ($J = 8 \rightarrow 7$ at 347.3 GHz) are both bright (average visibilities show a peak Stokes I of around 20 Jy/beam and 55 Jy/beam, respectively) and

both show Stokes V signals. The CO Stokes V signal has an antisymmetric structure. On the other hand, Figure 5 shows that the peak SiO Stokes V signal is purely negative. These lines (and others) are listed in Table 2 with their frequencies.

In IRC+10216 (Fig. 2) we again see Stokes V in the CO ($J = 3 \rightarrow 2$) but also in CS ($J = 7 \rightarrow 6$), SiS ($J = 19 \rightarrow 18$), and H¹³CN ($J = 4 \rightarrow 3$).

In NGC7538 (Fig. 3) the Stokes V signal in CO ($J = 3 \rightarrow 2$) at 345.8 GHz decreased in intensity after correction but is still prominent. There was also initially a very strong Stokes V signal in CH₂CO at 346.6 GHz that completely disappeared after correction.

Finally Figure 3 shows no detection in NGC1333, with only a clear detection of CO in Stokes I .

As mentioned previously, when assessing the Stokes V detections we consult the map for obvious pairs of positive/negative peaks that would indicate beam offset and therefore a potentially false Stokes V signal. The maps are integrated over a narrow frequency band of approximately 2 MHz so any peaks that exist are not washed out by noise in adjacent channels. In the maps for Orion KL and IRC+10216 shown in Figure 2 there are no negative peaks around the peak of Stokes V . However in NGC7538 there is quite a large negative Stokes V peak near our chosen peak that may indicate squint. The top panel of Figure 1 shows a typical appearance for squint signals which disappear after correction, and the pairs tend to resemble each other in shape. The pair of peaks around our chosen peak in NGC7538 however have distinct shapes. The worst case here is that the signal is entirely squint but on the other hand the signal may be a mixture of real and heavily affected by squint. The detections in Orion KL and IRC+10216 are more reliable.

5. DISCUSSION

The first question to address is whether our CP detections are real or result from instrumental artifacts. This is our chief concern because of the difficulty in calibrating CP measurements, especially since the observations presented here were not made with any special considerations for calibrating CP as in the observation of Sgr A* reported in Muñoz et al. (2012). We will repeat here the arguments made in Section 4 in support for the soundness of these detections, and then discuss earlier detections of CP and summarize how ARS can explain the detections presented in this work.

Firstly, we take the average of all the visibility data (not shown) and note that the peak Stokes V is not proportional to the peak Stokes I at any particular frequency. For example, a large Stokes I at 347.25GHz (SiO ($J = 8 \rightarrow 7$)) does not indicate a corresponding peak in Stokes V . This property indicates that there is

Object	Line	(GHz)	Stokes V (Jy/beam)
Orion KL	CO ($J = 3 \rightarrow 2$)	345.8	0.65
	SiO ($J = 8 \rightarrow 7$)	347.3	-0.65
NGC7538	CO ($J = 3 \rightarrow 2$)	345.8	0.85
IRC+10216	CS ($J = 7 \rightarrow 6$)	342.88	0.6
	SiS ($J = 19 \rightarrow 18$)	344.78	0.2
	H ¹³ CN ($J = 4 \rightarrow 3$)	345.34	0.8
	CO ($J = 3 \rightarrow 2$)	345.8	0.4
NGC1333 (IRAS2a)	CO ($J = 3 \rightarrow 2$)	345.8	-

Table 2. Summary of corrected Stokes V signals found. The beam size is determined by the configuration of the antennae array. An intensity for the peak of the Stokes V signal is only given if the peak is noticeably higher than the noise level. The intensity quoted for CO in NGC7538 is before smoothing is applied.

no systematic leakage of Stokes I into Stokes V , however excluding the longest baselines from the averaging does cause the Stokes V signals to follow Stokes I , pointing to some instrumental CP in the shortest baselines.

In the average visibilities (not shown) of Orion KL CO ($J = 3 \rightarrow 2$) and SiO ($J = 8 \rightarrow 7$) are the strongest lines, with the SiO ($J = 8 \rightarrow 7$) line the stronger. Therefore, if the Stokes V signal were purely leakage from Stokes I then we would expect to see an SiO Stokes V signal that is stronger than the CO Stokes V signal in the visibilities, but we do not; the Stokes V signal from CO ($J = 3 \rightarrow 2$) is stronger. This is also true in the visibilities of IRC+10216, where the CS ($J = 7 \rightarrow 6$) and SiS ($J = 19 \rightarrow 18$) lines have similar strengths but the Stokes V at SiS ($J = 19 \rightarrow 18$) is twice as intense. However, in the same object H¹³CN ($J = 4 \rightarrow 3$) and CO ($J = 3 \rightarrow 2$) have Stokes V intensities that appear proportional to their Stokes I intensity (i.e., stronger I means stronger V).

We also note that for Orion KL the shapes of the Stokes V signals vary across the frequency band and interpret this to mean that the signals are likely not instrumental in nature, assuming that any instrumental mechanism for producing spurious Stokes V produces a single type of CP (left or right). For example Figure 5 shows a spectrum for that source with Stokes V in CO and SiO. The SiO signal is purely negative (indicating only LCP) but the CO signal is antisymmetric, indicating the presence of both LCP and RCP. This has a physical explanation using the ARS model in terms of blue-shifted and red-shifted scattering populations that will be considered in Section 5.2. We know of no instru-

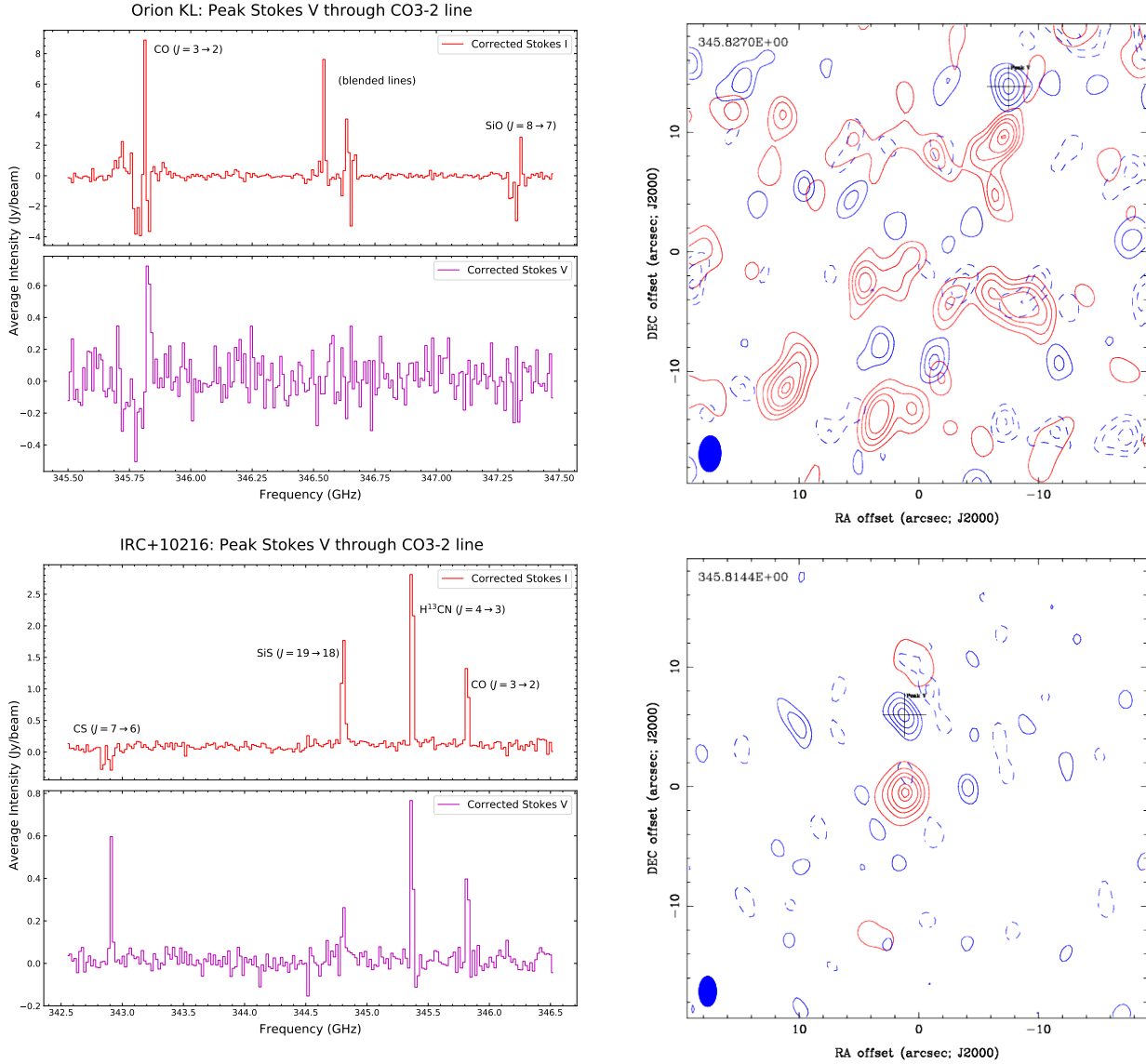


Figure 2. Corrected spectra and maps of the CO ($J = 3 \rightarrow 2$) line (345.8GHz) for Orion KL (top) and IRC+10216 (bottom). **Spectra:** *Miriad's maxfit* is used on the CO map to obtain the location on the image where the Stokes V signal at 345.8GHz is maximum, and a spectrum is obtained through that point. The cross on the map denotes the location of that peak. The red line is Stokes I and the blue is Stokes V . **Maps:** Blue contours are Stokes V and are shown at the -4, -3, -2, 2, 3, 4σ levels. The RMS error for each Stokes V map is found using *Miriad's imstat* command: $\sigma = 0.30$ and 0.17 Jy/beam, for Orion KL and IRC+10216, respectively. The distance of the peak to the phase center is $15''$ and $6''$, respectively. Dark red contours are Stokes I and the levels are 15%, 30%, 45%, 60%, 85% and 95% of the maximum. The value in the top left is the central frequency in GHz of the mapped signal, integrated over a narrow bandwidth of ~ 2 MHz.

mental mechanism for producing such a signature. For the other objects the Stokes V signal is always positive.

In the case of IRC+10216, an evolved carbon star with an extended envelope, the peak of Stokes V in the CO ($J = 3 \rightarrow 2$) map (bottom-right panel of Figure 2) is approximately $6''$ away from the Stokes I emission, which at first glance seems to point to an erroneous detection. However the real size of the CO envelope around IRC+10216 is much larger than seen here, as can be verified from single-dish CO ($J = 2 \rightarrow 1$) observations showing a circumstellar shell with a radius of about $50''$ (Fig. 1 of Cernicharo et al. 2015).

Spatial filtering due to the resolution of the interferometer explains the smaller spatial extent of IRC+10216

in the observations presented here and also explains the frequent occurrences of negative Stokes I in almost all the spectra shown in Figures 2, 3, and 5, as well as the high levels of CP ranging from 6% to 30%. The largest resolvable scale by an interferometer is determined by the length of the shortest baseline, meaning that large scale emission can be filtered out by the interferometer. For example in Orion KL the CO ($J = 3 \rightarrow 2$) Stokes I emission is large and extended (Hull et al. 2014). If the Stokes V signal came from smaller localized areas, then we would observe peaks of Stokes V as shown while only a portion of the Stokes I signal would be present. The rest of the Stokes I signal would be filtered away, which could shift the zero-level downward. Fluctuations in Stokes

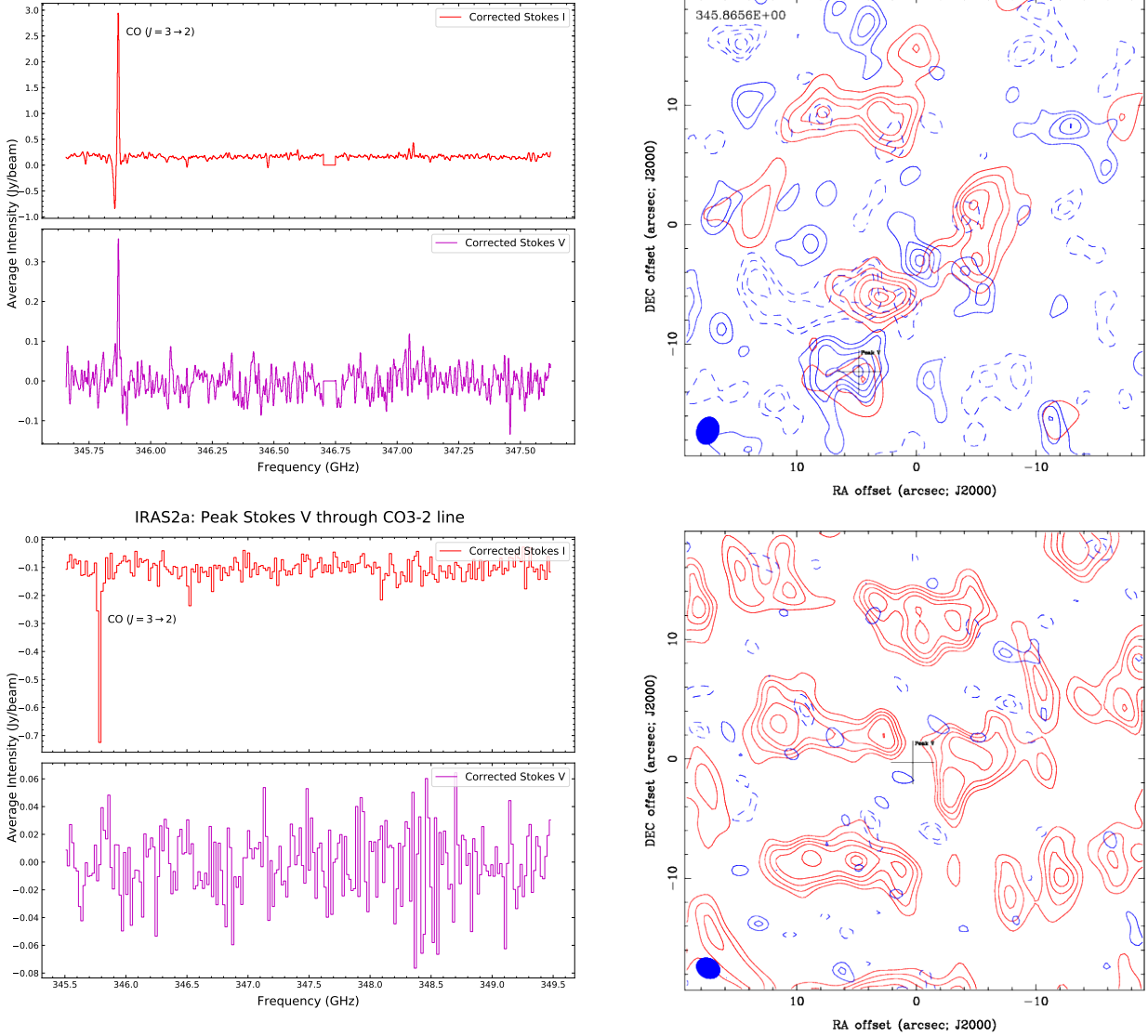


Figure 3. Same as Figure 2 but for NGC7538 (top) and NGC1333 IRAS2A (bottom). The spectrum for NGC7538 is Hanning smoothed. No significant Stokes V signal is detected in NGC1333 IRAS2A, probably because the object is too dim. Contours are the same levels as in Figure 2 and the spectrum is obtained the same way. The RMS for the NGC7538 and NGC1333 IRAS2A maps is $\sigma = 0.15$ and 0.12 Jy/beam, respectively. The distance of the peak to the phase center is $13''$ for NGC7538.

I could then appear to have negative values, while the weaker Stokes I could also explain the high levels of V/I observed.

Since the Stokes V features shown in the maps of Orion KL and IRC+10216 are compact we made maps excluding the shortest baselines, which have instrumental CP as shown from the averaging of the visibilities, and included only the longest baselines. If they are real, we expect the compact features to remain in these maps since the longest baselines have the highest resolution. We saw that the Stokes V peak remains in the maps of IRC+10216 after excluding more than half of the baselines as expected, however, the signal in Orion KL appears to disappear after excluding the shortest half of the baseline distances. This may indicate that the peak shown in Orion KL in Figure 2 is instrumental.

The level of instrumental CP is in general the

further the peak is from the center of the map since the instrumental polarization is found at the phase center. The peaks shown for Orion KL and NGC7538 (Figures 2 and 3) are several FWHMs of the beam away from the center, meaning the level of instrumental contamination in those peaks is likely higher.

Finally, we checked and confirmed that there were no Stokes V signals in the continuum comparable to those found in molecular lines like CO and SiO. In the continuum, V/I was found to be $<1\%$ for Orion KL and IRC+10216, and $<4\%$ in NGC7538. If the detected Stokes V originated from instrumental artifacts (other than I leakage) then we would expect to detect Stokes V at similar levels in the continuum, but this is not seen. The level of Stokes V found in molecular transitions is always higher than the level of Stokes V in the continuum for the observations presented here, and no

Stokes V Spectra before and after squint correction

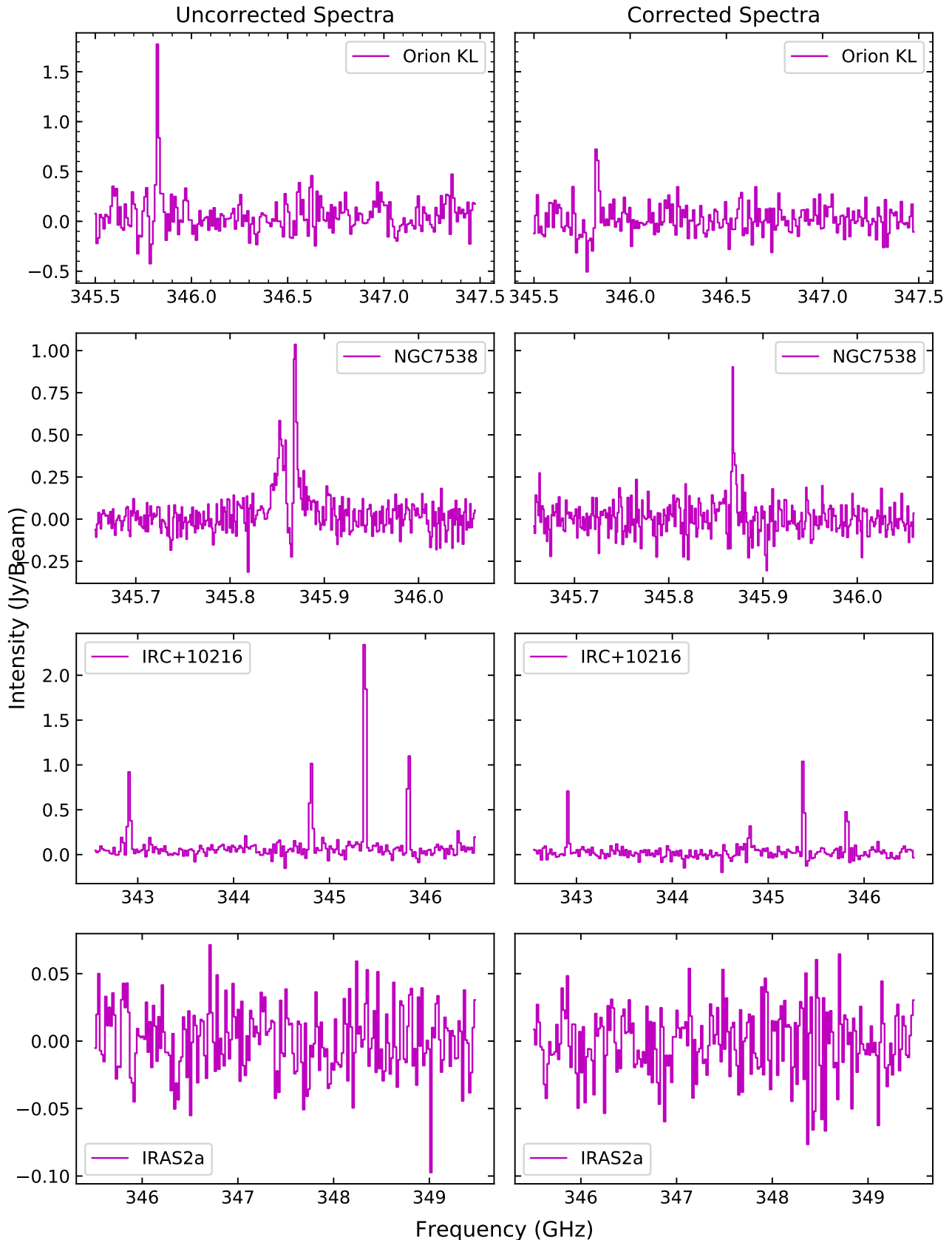


Figure 4. Stokes V spectra of all objects before and after squint correction. *Miriad's* `maxfit` is used on the CO map for each object to obtain the location in the image where the Stokes V signal at 345.8GHz is maximum, and a spectrum is obtained through that point. Note that the Stokes V signal decreases in all cases after squint correction. The location of the peak varies: sometimes it moves closer to the phase center after correction, sometimes further away.

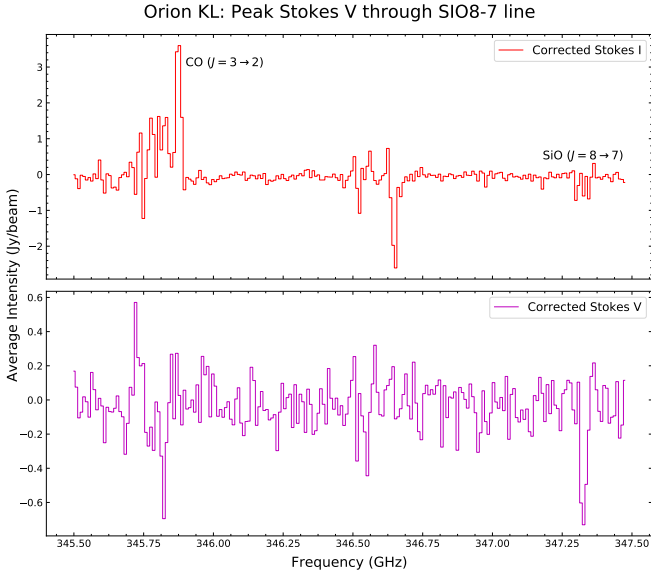


Figure 5. Peak Stokes V signal for the SiO ($J = 7 \rightarrow 8$ at 347.3 GHz) transition in Orion KL. Note there is also a strong Stokes V signal in the CO ($J = 3 \rightarrow 2$ at 345.8 GHz) transition here. The SiO signal is purely negative but the CO signal is antisymmetric.

significant Stokes V is found in the continuum.

We feel confident that the CP reported here, although perhaps suffering from some level of instrumental contamination, is real and originates from within these objects.

5.1. Earlier Non-Zeeman CP Detections

CP in a molecular spectral line weakly sensitive to the Zeeman effect was first reported by Houde et al. (2013), where approximately 2% polarization was detected in the ^{12}CO ($J = 2 \rightarrow 1$) transition at 230.5 GHz in Orion KL using the FSPPol at the CSO. The CP signal was approximately symmetric (i.e. “ \cap ”-shaped). The observation was repeated three months after the first measurement to confirm the result was not spurious, with similar results. Additionally the strong line of HCN ($J = 3 \rightarrow 2$) at 265.9 GHz in Orion KL was measured and no CP higher than the 0.1% level was detected. The detection in CO and the absence of a detection in HCN were evidence that the FSPPol/CSO observations were not significantly suffering from leakage into Stokes V and highlighted the CO molecule as a target for non-Zeeman CP. In all the objects presented here we find CP in ^{12}CO ($J = 3 \rightarrow 2$) at 345.8 GHz (except for in NGC1333 IRAS2A where the CO line is relatively weak). This is consistent with the original 2013 detection.

In follow up work Hezareh et al. (2013) examined the supernova remnant IC 443 using dust polarimetry with PolKa at APEX and polarization maps of ^{12}CO ($J =$

$2 \rightarrow 1$) and ($J = 1 \rightarrow 0$) taken with the IRAM 30m telescope. They initially found that the LP maps of dust and CO differed greatly in their polarization angles. Expecting that there was conversion of linear to circular polarization due to ARS, the CO Stokes V fluxes were then reinserted into the CO LP signals. The resulting CO polarization angle maps then agreed very well with each other, as well as with the dust map (Fig. 9 of Hezareh et al. 2013). This result clearly establishes a conversion from linear to circular polarization.

5.2. Anisotropic Resonant Scattering

ARS was the mechanism first proposed by Houde et al. (2013) to explain the presence of CP in the transitions of CO, but initially failed to explain the observed symmetric “ \cap ”-shaped Stokes V profile. In a follow up paper Houde (2014) considered observations of Stokes V in SiO masers (Cotton et al. 2011) and showed that different profile shapes detected are readily explained through ARS off populations of foreground molecules located slightly outside of the velocity range of the line. For example, a blue-shifted scattering population of molecules could result in a negative “ \cup ”-shaped profile while a red-shifted population in a positive “ \cap ”-shaped profile. The presence of both a blue- and red-shifted population would cause an antisymmetric “ S ”-shaped profile (like the one seen in the top left panel of Figure 2).

The basic principle of ARS can be illustrated by considering background LP radiation oriented at some angle θ to the foreground magnetic field. The incident and scattered radiation can be written in terms of the n -photon states as (Houde et al. 2013)

$$|\psi\rangle = \alpha|n_{||}\rangle + \beta|n_{\perp}\rangle \quad (5)$$

$$|\psi'\rangle \simeq \alpha e^{i\phi}|n_{||}\rangle + \beta|n_{\perp}\rangle, \quad (6)$$

where $\alpha = \cos(\theta)$, $\beta = \sin(\theta)$ and ϕ is a phase shift incurred after multiple scattering events. Following the definitions of the Stokes parameters and using an appropriate basis the Stokes parameters for the scattered radiation can be found to be

$$I = \alpha^2 + \beta^2 \quad (7)$$

$$Q = \alpha^2 - \beta^2 \quad (8)$$

$$U = 2\alpha\beta \cos(\phi) \quad (9)$$

$$V = 2\alpha\beta \sin(\phi). \quad (10)$$

This implies that in the chosen basis Stokes U is lost to Stokes V , i.e., more generally, LP is converted to CP. A calculation of the phase shift ϕ incurred due to ARS can be found in Houde et al. (2013).

Now, given a conversion from U to V it is clear that measuring V is necessary for techniques like the DCF method that rely on the dispersion of the PAs of LP to calculate the strength of the magnetic field. This

is because without corresponding V measurements, the PAs obtained from a molecular spectral line subject to ARS (like CO ($J = 3 \rightarrow 2$)) will be rotated according to

$$\tan(2\chi) = \cos(\phi) \tan(2\chi_0), \quad (11)$$

where χ_0 is the PA of the incident radiation and ϕ is the incurred phase shift as before (eq. 10 of Houde 2014), changing the dispersion of the PAs, as seen in Hezareh et al. (2013). As mentioned earlier, LP to CP conversion was reversed to obtain corrected polarization angles.

Because the DCF method relies on the observed dispersion of PAs using LP, any such studies using molecular lines must also include corresponding CP measurements to account for the polarization conversion effect and determine the correct orientation of the PAs (Hezareh et al. 2013; Chandrasekhar & Fermi 1953; Hildebrand et al. 2009; Houde et al. 2009).

6. CONCLUSION

We analyzed polarimetric observations from the SMA archive of Orion KL, IRC+10216, NGC7538 and

NGC1333 IRAS2A to search for CP signals. The data were corrected for squint, a source of spurious Stokes V signals that arises due to a slight misalignment in the beams used to obtain Stokes V when performing observations. We found evidence of significant Stokes V in Orion KL (in CO ($J = 3 \rightarrow 2$) and SiO ($J = 8 \rightarrow 7$)), in IRC+10216 (in CS ($J = 7 \rightarrow 6$), SiS ($J = 19 \rightarrow 18$), H¹³CN ($J = 4 \rightarrow 3$) and CO ($J = 3 \rightarrow 2$)) and in NGC7538 (in CO ($J = 3 \rightarrow 2$)). We measured relatively important levels of CP ranging from 6%-30%, probably due to the interferometric spatial filtering of large scale emission. No significant Stokes V was found in the continuum of any of the objects.

Theories that explain the presence of non-Zeeman CP in molecular spectral lines rely on the conversion of background LP to CP. The detections in multiple lines and objects presented here indicate that such an effect is likely widespread. Since the conversion of LP-to-CP modifies the observed dispersion of PAs, it is necessary to obtain precise measurements of CP along with LP for corresponding studies of the magnetic field in the interstellar medium.

REFERENCES

- Cernicharo, J., Marcelino, N., Agúndez M., Guélin, M. 2015
A&A, 575, A91
- Chandrasekhar, S., Fermi, E. 1953 ApJ, 118, 113
- Cortes, P. C., Crutcher, R. M., Watson, W. D. 2005, ApJ, 628, 780.
- Cotton, W. D., Ragland, S., Danchi, W. C. 2011, ApJ, 736, 96
- Crutcher, R. M. 2012 Annu. Rev. Astron. Astrophys, 50, 29-63
- Davis, L., Jr. 1951, PhRv, 81, 890
- Girart, J. M., Crutcher, R. M., Rao, R. 1999, ApJ, 525, L109.
- Girart, J. M., Patel, N., Vlemmings, W. H. T., Rao, R. 2012,
ApJ, 751, L20.
- Glenn, J., Walker, C. K., Biegling, J. H., et al. 1997, ApJ, 487, L89.
- Goldreich, P., Kylafis, N. D. 1981 ApJ, 243, L75-L78
- Greaves, J. S., Holland, W. S., Friberg, P., et al. 1999, ApJ, 512, L139.
- Hamaker, J. P., Bregman, J. D., Sault, R. J. 1996 A&A Suppl.
Ser., 117, 137-147
- Hezareh, T., & Houde, M. 2010, PASP, 122, 786
- Hezareh, T. J., Wiesemeyer, H., Houde, M., Gusdorf, A., Siringo, G. 2013 A&A, 558, A45
- Hildebrand, R. G., Kirby, L., Dotson, J. L., Houde, M.,
Vaillancourt, J. E. 2009 ApJ, 696, 567-573
- Houde, M., Vaillancourt, J. E., Hildebrand, R. H., Chitsazzadeh, S., Kirby, L., 2009 ApJ, 706, 1504
- Houde, M., Hezareh, T., Jones, S., Rajabi, F. 2013 ApJ, 764, 24
- Houde, M. 2014 ApJ, 795, 27
- Hull, C. L. H., Plambeck, R. L., Kwon, W., Bower, G. C.,
Carpenter, J. M., Crutcher, R. M., et al. 2014, ApJSuppl., 213, 13
- Hunter, J. D. 2007, Matplotlib: A 2D Graphics Environment,
Computing in Science & Engineering, 9, 3, 90-95
- Muñoz, D. J., Marrone, D. P., Moran, J. M., Rao, R. 2012 ApJ,
745, 115
- Marrone D. P., Rao R. 2008, Proc. SPIE 7020, 70202B
- Lai, S.-P., Girart, J. M., Crutcher, R. M. 2003, ApJ, 598, 392.
- Sault, R. J., Teuben, P. J. Wright, M. C. H. 1995 ADASS IV,
ASP Conference Series, 77, 433-436
- Sault, R. J., Hamaker, J. P., Bregman, J. D. 1996 A&A Suppl.
Ser., 117, 149-159
- Sault, R. J., Killeen, N. 2008, Miriad Users Guide, Australia
Telescope National Facility
- Schwab, F. R. 1980, Proc. SPIE 0231, Intl Optical Computing
Conf I
- Tang, Y.-W., Ho, P. T. P., Koch, P. M., Rao, R. 2010, ApJ, 717,
1262.
- Thompson, A. R., Moran, J. M., Swenson Jr, G. W. 2001,
Interferometry and synthesis in radio astronomy (John Wiley
& Sons)

4 Conclusion

To better understand the star formation process we seek to develop methods for accurately measuring the magnetic field in the interstellar medium. The easiest and most direct way to measure the magnetic field is spectrally and by exploiting the Zeeman splitting of certain molecular transitions. This method however has the disadvantage that most molecular species common in the ISM experience little to no Zeeman splitting, either because the magnetic field is not strong enough to split most lines or because of small Zeeman sensitivities for these molecules. The alternative to Zeeman splitting being developed over the last few decades is to perform polarimetry on either thermal dust emission in the continuum or on molecular spectral lines, which emit linearly polarized emission due to alignment with the magnetic field and, in the case of molecules, due to the Goldreich-Kylafis effect. There are several reasons one may want observations of molecular lines over dust emission, including greater information on cloud dynamics and three-dimensional cloud structure. Since the discovery of circular polarization in molecules weakly sensitive to the Zeeman effect reported in Houde et al. (2013), and the evidence that seems to indicate that the source of this CP is from the conversion of background LP as shown in Hezareh et al. (2013), it is important to determine how common this conversion effect is in order to limit false measurements of the magnetic field that rely solely on the Goldreich-Kylafis effect.

5 Acknowledgments

I would like to thank my supervisor Dr. Martin Houde for his advice and guidance during the last year and for sending me to Hilo, Hawaii for two weeks as soon as I finished my classes despite my having only a vague idea of what my project would entail and exactly zero research experience in Astronomy. Baptism by fire works.

I am also grateful to Dr. Ramprasad Rao and Prof. Josep Miquel Girart who not only made my visit to Hilo productive but also warm and fun. Thank you Josep Miquel and Miquel for accompanying me on my last-minute drive up Mauna Kea the night before our respective flights.

I am grateful to my friends, roommates, and the rock climbing crew for giving me things to do that are happily unrelated to work.

6 References

- Andersson, B-G., Lazarian, A., Vaillancourt, J. E. 2015, ARAA, 53, 501-39
- Carroll, B. W., Ostlie, D. A. 2006 Pearson, *An Introduction to Modern Astrophysics*. 2nd ed.
- Chandrasekhar, S., & Fermi, E. 1953 ApJ, 118, 113
- Cortes, P. C., Crutcher, R. M. & Watson, W. D. 2005, ApJ, 628, 780.
- Cotton, W. D., Ragland, S., & Danchi, W. C. 2011, ApJ, 736, 96
- Crutcher, R. M. 2012 Annu. Rev. Astron. Astrophys, 50, 29-63
- Davis, L., Jr. 1951, PhRv, 81, 890
- Girart, J. M., Crutcher, R. M. & Rao, R. 1999, ApJ, 525, L109.
- Girart, J. M., Rao, R., Marrone, D. P. 2006 Science, 313, 5788, 812-814
- Girart, J. M., Patel, N., Vlemmings, W. H. T., & Rao, R. 2012, ApJ, 751, L20.
- Glenn, J., Walker, C. K., Bieging, J. H., et al. 1997, ApJ, 487, L89.
- Goldreich, P., Kylafis, N. D. 1981 ApJ, 243, L75-L78
- Greaves, J. S., Holland, W. S., Friberg, P., et al. 1999, ApJ, 512, L139.

- Hamaker, J. P., Bregman, J. D., & Sault, R. J. 1996 A&A Suppl. Ser., 117, 137-147
- Hezareh, T., & Houde, M. 2010, PASP, 122, 786
- Hezareh, T. J., Wiesemeyer, H., Houde, M., Gusdorf, A., Siringo, G. 2013 A&A, 558, A45
- Hildebrand, R. G., Kirby, L., Dotson. J. L., Houde, M., Vaillancourt, J. E. 2009 ApJ, 696, 567-573
- Högbom, J. A. 1974 Astron. Astrophys. Suppl., 15, 417-426
- Houde, M., Vaillancourt, J. E., Hildebrand, R. H., Chitsazzadeh, S., & Kirby, L., 2009 ApJ, 706, 1504
- Houde, M. 2004, ApJ, 616, L111-L114
- Houde, M., Hezareh, T., Jones, S., & Rajabi, F. 2013 ApJ, 764, 24
- Houde, M. 2014 ApJ, 795, 27
- Hull, C. L. H., Plambeck, R. L., Kwon, W., Bower, G. C., Carpenter, J. M., Crutcher, R. M., et al. 2014, ApJ Suppl., 213, 13
- Hunter, J. D. 2007, Computing in Science & Engineering, 9, 3, 90-95
- Lai, S.-P., Girart, J. M. & Crutcher, R. M. 2003, ApJ, 598, 392.
- Muñoz, D. J., Marrone, D. P., Moran, J. M., & Rao, R. 2012 ApJ, 745, 115
- Marrone, D. P. & Rao, R. 2008, Proc. SPIE 7020, 70202B
- Miettinen, O. May 2007 “Zeeman effect - Studying Magnetic Fields in Star-Forming Regions”, slide show, University of Helsinki
- Nakano, T., Nakamura, T. 1978 Publ. Astron. Soc. Japan 30, 671-679

- Sault, R. J., Teuben, P. J. & Wright M. C. H. 1995 ADASS IV, ASP Conference Series, 77, 433-436
- Sault, R. J., Hamaker, J. P., & Bregman, J., D. 1996 A&A Suppl. Ser., 117, 149-159
- Sault, R. J., Killeen, N. 2008, Miriad Users Guide, Australia Telescope National Facility
- Schwab, F. R. 1980, Proc. SPIE 0231, Intl Optical Computing Conf I
- Tang, Y.-W., Ho, P. T. P., Koch, P. M., & Rao, R. 2010, ApJ, 717, 1262.
- Thompson, A. R., Moran, J. M., & Swenson Jr, G. W. 2001, Interferometry and synthesis in radio astronomy (John Wiley & Sons)
- Vanderlinde, K. July 2017 “Radio Telescope Fundamentals”, slide show, Dunlap Summer School
- Zeeman, P. 1897, ApJ, 5, 332